International Journal of Heat and Mass Transfer 171 (2021) 121099

Contents lists available at ScienceDirect

International Journal of Heat and Mass Transfer

journal homepage: www.elsevier.com/locate/hmt

Numerical analysis of direct contact condensation-induced water hammering effect using OpenFOAM in realistic steam pipes

T.Q.D. Pham, Sanghun Choi*

School of Mechanical Engineering, Kyungpook National University, Daegu, South Korea

ARTICLE INFO

Article history:
Received 13 October 2020
Revised 8 February 2021
Accepted 10 February 2021

Keywords:
Computational fluid dynamics
Condensation
InterFoam
Lee model
Phase change
Tanasawa model
Volume of fluid model

ABSTRACT

Direct contact condensation (DCC)-induced water hammer in a horizontal pipe is an important phenomenon observed in many industrial fields such as nuclear and thermal engineering. This study aims to simulate the DCC-induced water hammering effect in previously designed steam pipes. The numerical simulation for the water hammering was performed in our computational fluid dynamics (CFD) solver modified from interFoam included in the open-source software OpenFOAM v.6. The new solver includes an energy equation and existing phase change models. Computational domains were reconstructed using our Python-based semiautomated mesh-generation algorithm to investigate local variations of temperature and pressure inside a steam pipe. Continuity, momentum, and energy equations of a volume of fluid model were discretized using the pressure-implicit method for the pressure-linked equation algorithm. Implicit Euler and central difference schemes were used for temporal and spatial discretization, respectively. The CFD solver with the phase change model was validated using a one-dimensional Stefan problem's benchmark case. In a PMK-2 steam pipe, the temperature drop due to the water hammering was temporally consistent with the existing experimental result. A smaller pressure was captured in the region where the phase change of steam to water was observed. This induced an adverse pressure gradient that drove the water moving backward, resulting in water hammering. The water hammering was further investigated by changing the water temperature and flow rate in a different steam pipe. A higher water flow rate (i.e., large Froude number) was found to dampen the steam pipe's pressure shock.

© 2021 Elsevier Ltd. All rights reserved.

1. Introduction

Heat and mass transfers due to a phase change from water to vapor are common in many industrial systems [1-5]. Such a phase change on the interface can trigger a water hammer in nuclear thermal–hydraulic systems, which may lead to a fracture or failure of the hydraulic system. For instance, during coolant loss, cold water could be injected into the curved region of steam pipes near the reactor vessel to cool overheated steam pipes. This setting is called the emergency core cooling system (ECCS) [6]. During the cooling process, depending on the steam generator feed-water inlet design, auxiliary cold water can be injected through a horizontal pipe into the steam generator. If this steam generator has a low water level, a water hammer event can be triggered by direct contact condensation (DCC). When an entrapped gas bubble suddenly collapses because of strong turbulence and subcooling of the water phase, the saturated water forms a "bullet" that rushes at high speed into the joint of the pipe. This creates a loud bang like a hammer hitting, squeezing, and stretching the pipe, called condensation-induced water hammer (CIWH). This considerably elevates the steam pipe's local pressure, which causes massive damage to the power plant system; this may result in economic loss and safety risks.

To describe water hammering using computational fluid dynamics (CFD), Štrubelj et al. [7] performed numerical simulations using their computer code NEPTUNE_CFD along with the two-fluid model in the horizontal steam pipe. The case was named PMK-2 [8], experimentally designed by the Hungarian Atomic Energy Research Institute (KFKI). They demonstrated that the slow flooding of the pipe was abruptly interrupted by a strong slugging, followed by inducing pressure surges induced by the water hammer. The "NEPTUNE_CFD" code could precisely capture the transition from stratified to slug flow based on the large interface model. In a similar study, Ceuca and his colleague [9,10] performed a numerical simulation at the experimental facility built at the University of

* Corresponding author at: School of Mechanical Engineering, Kyungpook National University, 80 Daehak-ro, Buk-gu, Daegu 41566, Republic of Korea.
E-mail addresses: pqducthinhbka@gmail.com (T.Q.D. Pham), s-choi@knu.ac.kr (S. Choi).

https://doi.org/10.1016/j.ijheatmasstransfer.2021.121099
0017-9310/© 2021 Elsevier Ltd. All rights reserved.

Nomenclature

A_D	diagonal entries of the momentum matrix equation, m^{-3} s^{-1}
c_p	specific heat, J kg^{-1} K^{-1}
$C_{1\varepsilon}$	k-ε model constant-1 (1.44), dimensionless
$C_{2\varepsilon}$	k-ε model constant-1 (1.92), dimensionless
D	pipe diameter, m
Fr	Froude number, dimensionless
$\mathbf{f_\sigma}$	surface tension force in a unit volume, N m^{-3}
$\mathbf{g}$	gravitational acceleration vector (0, −9.81, 0), m s^{-2}
G	effective production, m^2 s^{-3}
h	water height, m
H_{fg}	latent heat, J kg^{-1}
k_e	turbulent kinetic energy, m^2 s^{-2}
k	thermal conductivity, W m^{-1} K^{-1}
M	molar mass, kg mol^{-1}
$\dot{m}''$	net mass flux, kg m^{-2} s^{-1}
$\dot{m}'''$	mass transfer rate in a unit volume, kg m^{-3} s^{-1}
p	static pressure, Pa
p'	corrected pressure in OpenFOAM, Pa
Q	volume flow rate, L s^{-1}
R^2	Coefficient of determination, dimensionless
R	universal gas constant, J kg^{-1} K^{-1}
Re	Reynolds number, dimensionless
t	time, s
T	temperature, K
$\mathbf{u}$	fluid velocity vector, m s^{-1}
$\mathbf{u_s}$	artificial velocity vectors, m s^{-1}
U	average magnitude of water velocity, m s^{-1}
y^+	characteristic length of wall-adjacent cells, dimensionless

Greek symbols

α	volume fraction, dimensionless
α_{vd}	vapor thermal diffusivity, m^2 s^{-1}
β	mass transfer intensity factor, s^{-1}
γ	accommodation factor, dimensionless
ε	dissipation rate, J kg^{-1} s^{-1}
λ	dimensionless parameter in the Stefan problem, dimensionless
μ	fluid dynamic viscosity, kg m^{-1} s^{-1}
ν	fluid kinematic viscosity, m^2 s^{-1}
ρ	fluid density, kg m^{-3}
σ	turbulent Prandtl number, dimensionless

Abbreviations/subscripts/suffixes

CIWH	condensation-induced water hammer
CFD	computational fluid dynamics
DCC	direct contact condensation
ECCS	emergency core cooling system
KFKI	Hungarian Atomic Energy Research Institute
total	total time
PISO	pressure-implicit with splitting operators
SIMPLE	semi-implicit method for pressure-linked equations
PIMPLE	pressure-implicit method for pressure-linked equations
sat	saturation
v	vapor
vw	vapor to water
VOF	volume of fluid
w	water
wv	water to vapor

Technology in Germany using different models (named Fr03T40, Fr06T40, and Fr06T60). They validated the "ATHLET" system code and also apparently showed that different Reynolds numbers (Re) and Froude numbers (Fr) between two phases could affect the DCC-driven condensation events. In another study, Priyankan Datta et al. [11] proposed a dedicated one-dimensional (1D), compressible in-house code formulated based on the two-fluid model to explore the underlying physics of the CIWH phenomenon in a horizontal steam pipe. Further, Höhne et al. [12] investigated the condensation phenomena inside the steam pipes developed by the Lithuanian Energy Institute. They evaluated three different phase change models, i.e., "Egorov DCC model [13]," "Hughes Duffey model [14]," and "Coste DCC model [15]" for the DCC scenario, and demonstrated good accuracy compared with their experiment results.

In the CFD-based prediction, a selection of physically precise models of the interfacial heat and mass transfers plays a vital role in simulating CIWH. Several heat and mass transfer models have been developed [16-21], but most of them were derived from the fundamental models introduced by Lee [22] and Tanasawa [23]. Seven decades ago, Schrage [24] developed a phase change model considering the pressure difference between the two phases, where the mass flux was calculated from the mass balance at the interface. The initial model developed by Schrage [24] was somewhat complicated; therefore, Tanasawa [23] simplified it by assuming constant saturation temperatures at both sides of the interface. Moreover, Lee [22] introduced a phase change model based on the other modifications of the Schrage model, assuming that mass transfer due to boiling and condensation occurs under constant pressure across the interface. This implies that the phase change occurs mainly because of the temperature difference between the two phases. Later, it was modified by Chen et al. [25] using different empirical coefficients. The models proposed by Lee and Tanasawa are similar with regard to heat and mass transfers being computed by the temperature difference between phases.

The selection and use of heat transfer models play an important role in predicting the DCC-induced water hammer. However, to the best of our knowledge, few studies have used the heat transfer models by Lee and Tanasawa to describe the water hammering phenomenon inside existing experimental devices. Against this background, this study aims to investigate the DCC-induced water hammer using the open-source software OpenFOAM. For this, we first modified and extended the existing volume of fluid (VOF) solver named interFoam to solve the energy equation, including heat and mass transfer models. Next, the new CFD solver was validated using the well-known benchmark problem, i.e., 1-D condensation and evaporation Stefan problems. Then, the PMK-2 experimental facility was used to perform the DCC-induced water hammer using this solver. Finally, we further solved an additional steam pipe case provided by our partner company, Korea Electric Power Corporation (KEPCO). By changing numerical conditions such as flow rate and water temperature, the numerical parameters, including temperature and pressure, were measured at two different locations. We also utilized our semiautomatic mesh generator to construct nonuniform meshes for quantitative analysis.

2. Numerical methods

To mimic the CIWH, we employed the open-source library OpenFOAM v.6, which is based on the finite volume method for solving incompressible Navier–Stokes equations. The present solver was implemented in the framework of the interFoam solver (base solver) provided in OpenFOAM. A thermal energy transport equation was added to the base solver. We then added source terms associated with the phase change to volume fraction transport equation and momentum equation. The interface between the two phases was resolved using an interface capturing method of VOF.

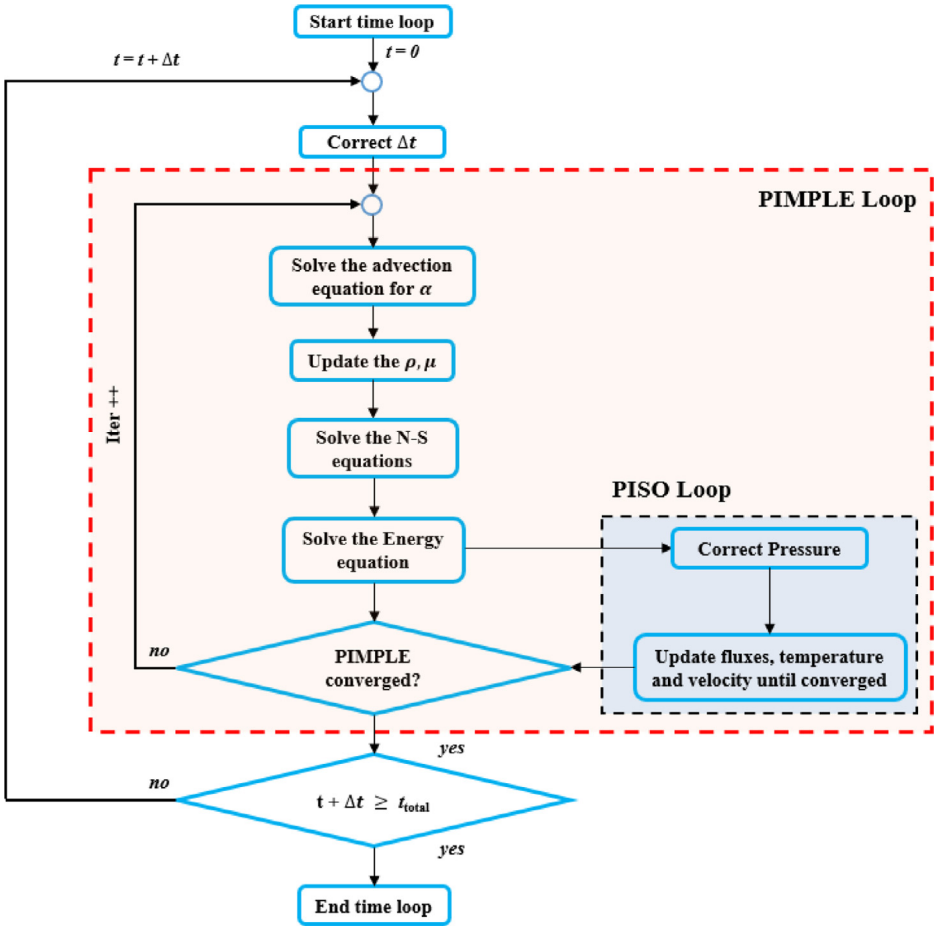

Fig. 1. Flowchart of the interFoam extended solver in the open-source software OpenFOAM.

The pressure-implicit method for pressure-linked equations algorithm (PIMPLE) was employed to obtain transient pressure and velocity fields. For the discretization of the convective terms in the momentum and phase equations, we used the limited linear and van Leer schemes, respectively. The present solver and the numerical characteristics of two-phase change models are described below.

2.1. Governing equations and implementation

Our phase change solver was extended from the isothermal two-phase flow solver, the so-called interFoam described in [26]. To demonstrate the performance of the two numerical phase change models, i.e., Lee and Tanasawa, we implemented both models in this solver. The overall algorithm could be summarized in the form of the following steps, along with Fig. 1:

1. Define vector and scalar fields of velocity vector **u**, static pressure p, temperature T, and volume fraction α. Note that interFoam solves pressure p' corrected for hydrostatic variation, computed as $p' = p - \rho g h$, where ρ, g, and h are the water density, gravitational acceleration, and water height, respectively. Pressure correction is used to avoid any sudden changes in the pressure at the boundaries for hydrostatic effects.
2. Start the time loop and solve the advection equation of the volume fraction α:

$$\frac{\partial \alpha}{\partial t} + \nabla \cdot (\mathbf{u}\alpha) + \nabla \cdot [\mathbf{u_s}\alpha(1-\alpha)] = 0, \tag{1}$$

where **u** and $\mathbf{u_s}$ are the velocity and artificial velocity vectors, respectively, used to confine α between 0 and 1 [27]. Eq. (1) was solved using the multidimensional universal limiter with an explicit solution method, where an additional limiter was used to cut off the face-fluxes at the critical values.

3. Update the fluid physical properties of ρ and dynamic viscosity μ, based on α, using the following equations:

$$\rho = \alpha\rho_1 + (1-\alpha)\rho_2, \tag{2}$$

$$\mu = \alpha\mu_1 + (1-\alpha)\mu_2, \tag{3}$$

where ρ_1, ρ_2, μ_1, and μ_2 are the fluid density of phase 1 (vapor), fluid density of phase 2 (water), fluid dynamic viscosity of phase 1, and fluid dynamic viscosity of phase 2, respectively.

4. Solve incompressible Navier–Stokes equations with phase change between water and vapor phases defined as follows:

$$\frac{\partial(\rho\mathbf{u})}{\partial t} + \nabla \cdot (\rho\mathbf{u}\mathbf{u}) = -\nabla p' + \nabla \cdot \left[\left(\nabla\mathbf{u} + \nabla\mathbf{u}^T\right)\right] + \rho\mathbf{g} + \mathbf{f}_\sigma, \tag{4}$$

$$\nabla \cdot \left(\frac{1}{A_D}\nabla p'\right) = \nabla \cdot \mathbf{u} - \dot{m}'''\left(\frac{1}{\rho_2} - \frac{1}{\rho_1}\right), \tag{5}$$

where $\mathbf{g}$, $\mathbf{f}_\sigma$, A_D, and $\dot{m}'''$ are the gravitational acceleration vector, surface tension force, diagonal entries of the momentum matrix equation, and mass flow rate per unit volume, respectively. The continuity equation is enforced by solving the Poisson pressure equation (Eq. (5)).

5. Solve the energy equation for temperature, which is added in the present solver as follows:

$$\frac{\partial(\rho c_p T)}{\partial t} + \nabla \cdot (\rho c_p \mathbf{u} T) - \nabla \cdot (k \nabla T) = -\dot{m}''' H_{fg}, \quad (6)$$

where c_p, H_{fg}, and k are the specific heat at constant pressure, latent heat, and thermal conductivity, respectively. This equation can be numerically solved if adequate boundary conditions are defined at the system boundaries.

6. Correct the pressure, fluxes, temperature, and velocities using PIMPLE loop:

   PIMPLE combines pressure-implicit with splitting operators (PISO) with the semi-implicit method for pressure-linked equations (SIMPLE) to correct the pressure together with nonlinear iterations. The convergence criteria for the PIMPLE loop in this study are based on a fixed number of iterations ($N = 2$, default). PIMPLE is known to provide more stable results than PISO because it uses SIMPLE-based nonlinear iterations instead of a predictor-correction step.

7. Move to the next time step (starting from step 2). The overall flowchart of the modified interFoam solver is briefly described in Fig. 1.

2.2. Phase change model

2.2.1. Lee model

The model introduced by Lee calculates the mass transfer rate of phase change processes in both evaporation and condensation. The Lee model is based on the assumption that phase change occurs under constant pressure conditions. The mass flow rate per unit volume is defined as

$$\dot{m}'''_{wv} = \beta_1 \alpha_1 \rho_1 \frac{(T_w - T_{sat})}{T_{sat}}, \quad (7)$$

$$\dot{m}'''_{vw} = \beta_2 \alpha_2 \rho_2 \frac{(T_{sat} - T_v)}{T_{sat}}, \quad (8)$$

where T_w, T_v, T_{sat}, β_1, and β_2 indicate the water temperature, vapor temperature, saturation temperature, and mass transfer intensity factor of the vapor and water phases, respectively. Both β_1 and β_2 were set to 0.1–10^7 according to Lee's research.

2.2.2. Tanasawa model

Unlike the Lee model, the Tanasawa model assumes that the interfacial temperature is equal to the saturation temperature and the heat flux is linearly dependent on the temperature jump between the interface and the vapor. The net mass flux is expressed as

$$\dot{m}''_{wv} = \frac{2}{2-\gamma}\sqrt{\frac{M}{2\pi R}}\frac{\rho_v H_{fg}(T_w - T_{sat})}{T_{sat}^{1.5}}, \quad (9)$$

$$\dot{m}''_{vw} = \frac{2}{2-\gamma}\sqrt{\frac{M}{2\pi R}}\frac{\rho_v H_{fg}(T_{sat} - T_v)}{T_{sat}^{1.5}}, \quad (10)$$

where γ, M, and R are the accommodation factor, molar mass, and universal gas constant, respectively. In our simulation, they were set to 1, 0.018 kg/mol, and 8.314 J/mol·K, respectively. The mass flow rates per unit volume were then calculated using the following formula for liquid-to-vapor and vapor-to-liquid, respectively:

$$\dot{m}'''_{wv} = \dot{m}''_{wv}|\nabla \alpha_w|, \quad (11)$$

$$\dot{m}'''_{vw} = \dot{m}''_{vw}|\nabla \alpha_v|, \quad (12)$$

where the Gaussian linear method using Gaussian quadrature (interpolation) and central difference scheme (gradient) was used to compute the gradient of water and vapor volume fractions.

2.3. Turbulence model

The standard k–ε turbulence model [28] was used to resolve the turbulence behavior in the steam pipes. Two equations are solved for the turbulent kinetic energy k_e and dissipation rate ε:

$$\frac{\partial}{\partial t}(\rho k_e) + \nabla \cdot (\rho \mathbf{u} k_e) = \nabla \cdot \left[\left(\mu + \frac{\mu_t}{\sigma_{k_e}}\right)\nabla k_e\right] + G_{k_e}, \quad (13)$$

$$\frac{\partial}{\partial t}(\rho \varepsilon) + \nabla \cdot (\rho \mathbf{u} \varepsilon) = \nabla \cdot \left[\left(\mu + \frac{\mu_t}{\sigma_\epsilon}\right)\nabla \varepsilon\right] + C_{1\varepsilon}\frac{\varepsilon}{k_e}\left(G_{k_e} + C_{3\varepsilon} G_b\right) - C_{2\varepsilon}\rho\frac{\varepsilon^2}{k_e}, \quad (14)$$

where G, σ, and C are the effective production, turbulent Prandtl number, and model constant, respectively. In this study, the Prandtl numbers σ_k and σ_ε and model constants $C_{1\varepsilon}$ and $C_{2\varepsilon}$ were set to 1.0, 1.3, 1.44, and 1.92, respectively.

2.4. Description of the experimental devices

2.4.1. PMK-2 experimental device

Fig. 2 shows an experimental device operated at the KFKI. This experimental device was named PMK-2 [8] in the WAHALoads project of the 5th European Union research program. This project aimed at describing the water hammering effect using the 1-D two-fluid model and the WAHA code. The pipe geometry is a 2870-mm-long horizontal linear part and a 1007-mm-long vertical linear pipe with an inner diameter of 73 mm. The steam generator supplies vapor through the inlet head of a 90° bend, extending to the horizontal pipe. On the other end, cold water with a temperature of 295 K and a flow rate of 1.7 kg/s is injected through the curved pipe of the bottom of the vertical steam-line section, which results in Re = 29,209 and Fr = 0.53. Re and Fr were computed as UD/ν and $U/(gD)^{0.5}$, respectively, where U, D, and ν indicate the average water velocity, pipe diameter, and water kinematic viscosity, respectively. CIWH occurred in the horizontal pipe, as expected, by the turbulent Re of 10,000 [7]. Cold water supply was obtained from a 75-L water tank pressurized with nitrogen and connected to the bottom of the vertical steam-line section below the water inlet heat. Before the start of the experiment, the entire setup was heated with steam for a few hours. More details about the experiment setup can be found in [8]. According to Prasser et al. [8], 35 water hammer experimental results were obtained from the PMK-2 experiments with different conditions. These results were obtained through three types of sensors: a wire-mesh sensor, a temperature sensor, and three pressure transducers. Their specific locations are shown in Fig. 2. In addition, Table 1 lists the numerical settings and boundary conditions of the computational simulation.

2.4.2. KEPCO experimental device

We presented an additional realistic water hammering case designed at KEPCO. The bundle of steam pipes in the experimental facility has an elaborate setup from a design drawing. Fig. 3 depicts a three-dimensional schematic of a steam pipe. The water hammer phenomenon was mimicked under the conditions similar to those in the PMK-2 experiment. The KEPCO test section imposed the subcooled water at 295 K similar to the PMK-2 case. A volumetric flow rate of 0.1 m^3/s was supplied to the test section containing the saturated steam at an initial system pressure of 1.45 MPa, resulting in Re = 277,394 and Fr = 0.29. The test rig had an internal pipe diameter of 459 mm. From an instrumentation point of view, the test section was equipped with two temperature and pressure sensors along the mainstream, such that those were extracted at the two measuring points located at 4 and 10 m (Fig. 3) from the horizontal upward pipe. Table 1 lists the numerical settings and boundary conditions of the computational simulation.

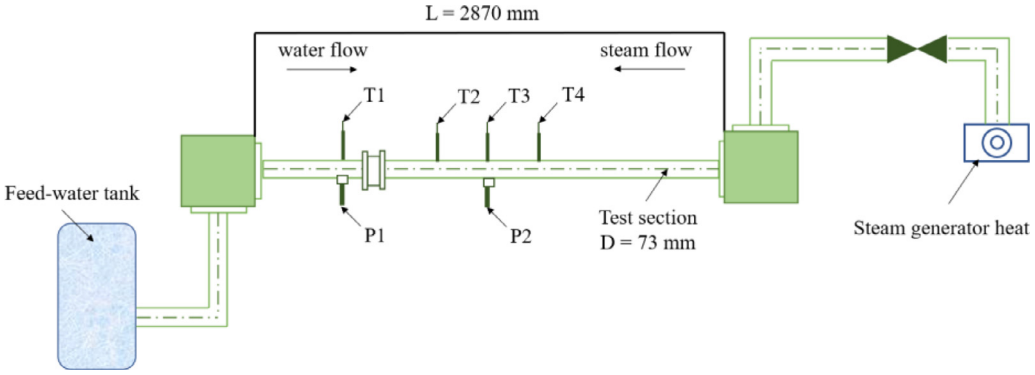

Fig. 2. Simplified schematic representation of the PMK-2 experimental device [8].

Table 1
Numerical settings and boundary conditions of the computational simulations.

			Settings/Description
Numerical solver in OpenFOAM			interFoam extended
Two-phase flow model			Volume of fluid
Time step			1×10^{-5} s
Max CFL (Courant-Friedrichs-Lewy) number			0.5
Total time			20 s for the PMK-2 case 100 s for the KEPCO case
Prandtl number			0.7
Boundary conditions	**Inlet**	Temperature	Fixed value (295 K)
		Velocity (Flow-rate)	Uniform flow rate (1.7 kg/s for the PMK-2 case, 0.1 m^3/s for the KEPCO case)
	Outlet	Temperature	Zero gradient if fluid flows out, and fixed value if fluid flows into the domain
		Velocity	Zero-gradient velocity
	Wall	Temperature	Fixed value (470 K)
		Velocity	No-slip velocity

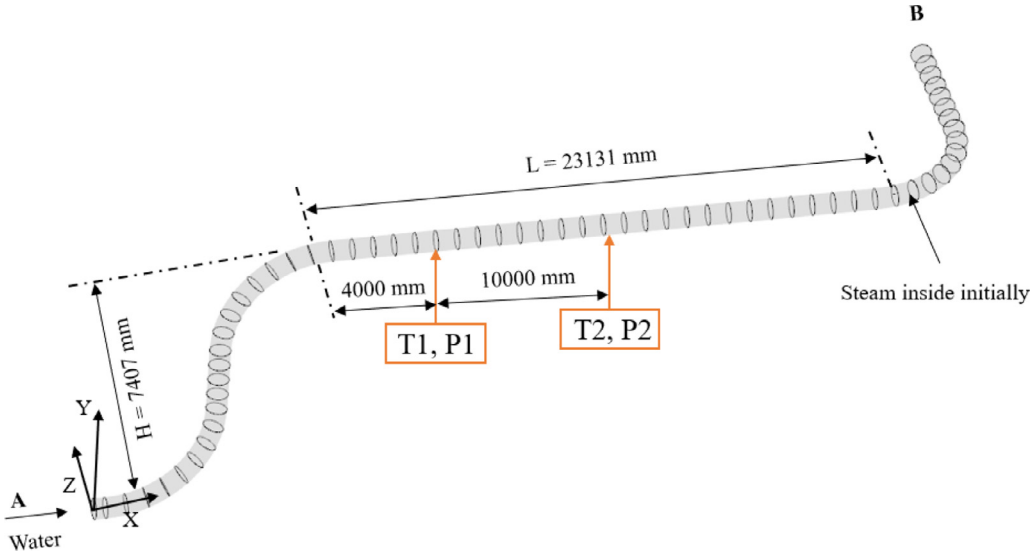

Fig. 3. Schematic representation of the test section of KEPCO's realistic experimental facility.

2.5. Mesh generation

To construct a straight and curved pipe comparable with the experimental setting, we employed the 1-D centerline-based mesh-generation algorithm [29]. This approach is beneficial when performing a regional assessment in a subdomain. The centerline of the pipe direction was drawn using the open-source computer-aided design program FreeCAD. Then, the 1-D geometry was achieved by sweeping the centerline, as shown in Fig. 4(A). The 1-D centerline should be divided before meshing to obtain the separated surface and volume zones and intermediate cross-section face zones. The 1-D centerline was divided into several linear lines (Fig. 4(B)) using Python. Each line contains information on the radius of the cross section and divided line length, so we used the radius:length ratio to set the number of divided parts. Fig. 4(C) shows the final output before meshing. The bold red circles represent the edges of every cross-section zone, and the two cross lines are the cross section diameters for each orthogonal direction. We used the freeware mesh-generating software Gmsh [30] for the meshing after in-house division. Inlet, outlet, walls, divided volumes, and cross-section zones were generated at the pipe mesh after mesh generation. Fig. 4(D) shows a sample mesh of the entire

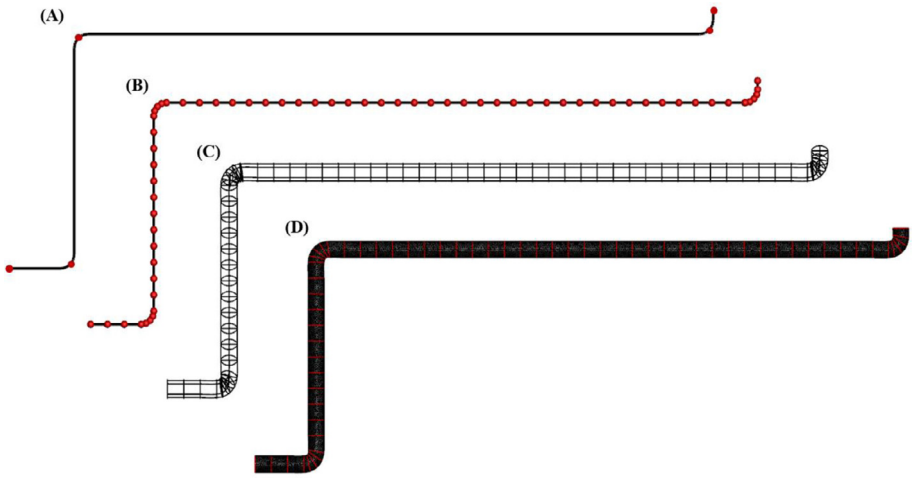

Fig. 4. Schematic representation of the PMK-2 geometry and mesh: (A) centerline from FreeCAD, (B) divided centerline and element number, (C) intermediate cross-section zones of the pipe before mesh generation, (D) mesh with cross-section zones.

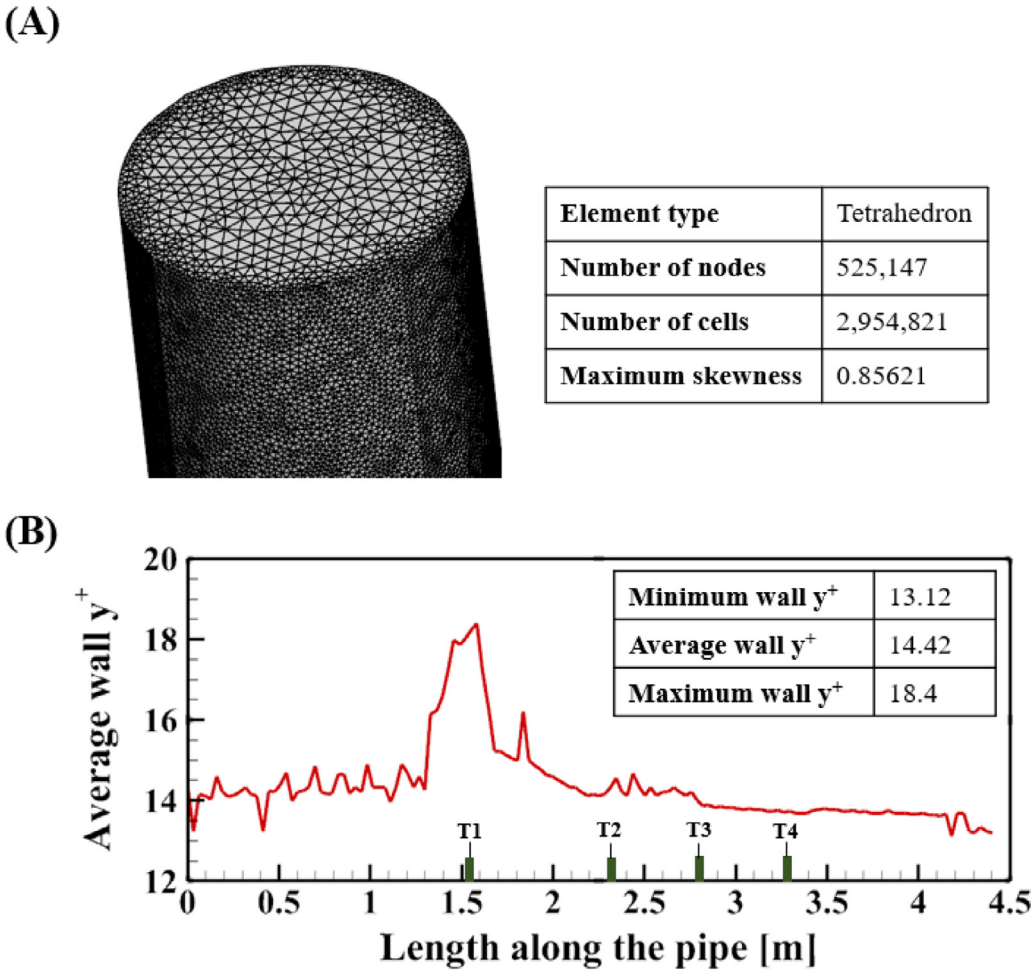

Fig. 5. (A) The medium-mesh characteristics at the horizontal steam pipe, and (B) the average wall y^+ along the steam pipe.

domain, and every volume zone is divided by each cross-section zone, shown as a red line. The overall meshing algorithm can be seen in detail in the previous study [29].

Fig. 5(A) shows the medium-mesh generated by our 1-D meshing algorithm and its characteristics. The non-uniform mesh is generated using a uniform background mesh (surface mesh) and the non-uniform grid size distribution (diameter, length, and ratio) with tetrahedral cells. The spatial resolution of the mesh is higher near wall regions to resolve the boundary layer, resulting in a maximum and minimum characteristic lengths of an element of 5.2 mm, and 0.78 mm, respectively. Besides, the maximum skewness is 0.85621, ensuring a sufficiently fine unstructured mesh to validate the prediction data. Fig. 5(B) shows the average wall y^+ along the length of the steam pipe. The maximum, minimum and

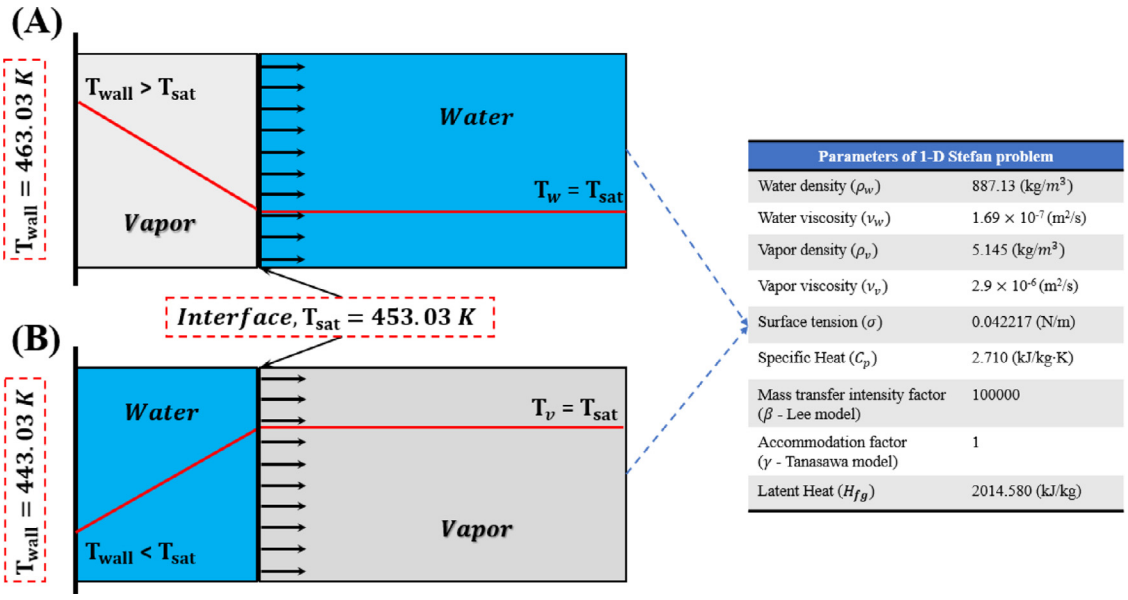

Parameters of 1-D Stefan problem	
Water density (ρ_w)	887.13 (kg/m^3)
Water viscosity (ν_w)	1.69×10^{-7} (m^2/s)
Vapor density (ρ_v)	5.145 (kg/m^3)
Vapor viscosity (ν_v)	2.9×10^{-6} (m^2/s)
Surface tension (σ)	0.042217 (N/m)
Specific Heat (C_p)	2.710 (kJ/kg·K)
Mass transfer intensity factor (β - Lee model)	100000
Accommodation factor (γ - Tanasawa model)	1
Latent Heat (H_{fg})	2014.580 (kJ/kg)

Fig. 6. Schematics and parameters of the (A) evaporation and (B) condensation Stefan problems.

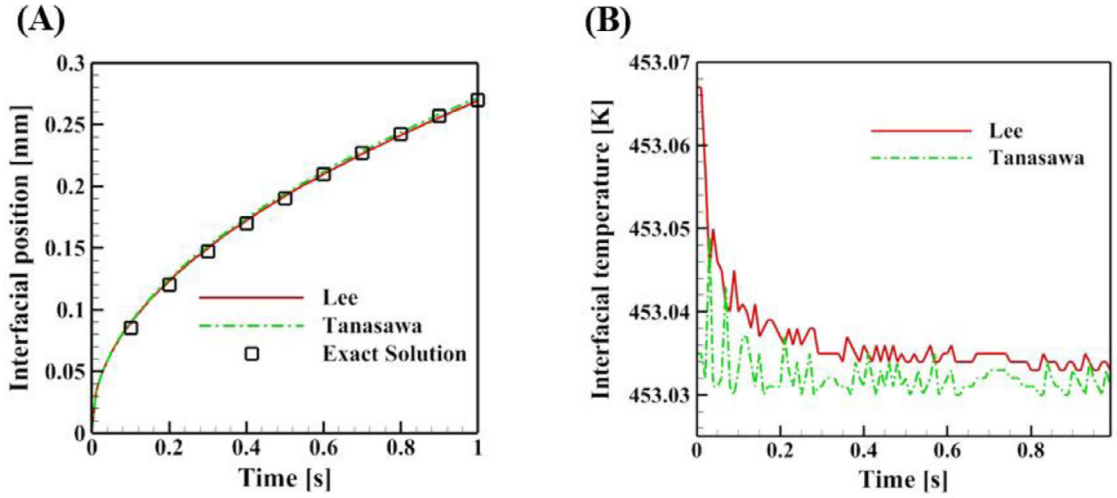

Fig. 7. Temporal result of the interfacial (A) position and (B) temperature for the evaporation Stefan problem.

average wall y^+ in the entire steam pipe are reported in the figure. The maximum $y+$ is observed near the T1 measurement point, corresponding to the region where the most significant water hammer appears. In addition, the unstructured mesh and structured mesh performance and mesh convergence study are shown in Section 3.2.

3. Results and discussion

3.1. Validation of the solver and comparison between the two-phase change models

In this section, to validate the present solver, two formal phase change phenomena (condensation and evaporation) were considered in the Stefan problem [31] because both the benchmark problems had analytical solutions. The isosurface of $\alpha = 0.5$ indicating the interface of two phases was used in the entire simulation for the visualization of both cases. In the evaporation case (i.e., water to vapor), a vapor film separates saturated water from a superheated wall; in the condensation case, a water film separates saturated vapor from a superheated wall. The analytical solution to this problem is

$$x(t) = 2\lambda\sqrt{\alpha_{vd}t}, \tag{15}$$

$$\lambda\exp(\lambda^2)\mathrm{erf}(\lambda) = \frac{C_p|T_w - T_{sat}|}{H_{fg}\sqrt{\pi}}, \tag{16}$$

where λ, $x(t)$, and α_{vd} are the dimensionless parameters obtained from Eq. (9)(b), the interfacial position from the wall, and the vapor thermal diffusivity, respectively. In this problem, the difference between the saturation and wall temperatures was set to $\Delta T = |T_w - T_{sat}| = 10$ K. Computational simulations were performed for a domain of length 0.4 mm with a 1-D uniform grid of 401 vertices, allowing a grid size of 0.001 mm. The properties of each phase and the schematic of the Stefan problem are provided in Fig. 6.

3.1.1. Evaporation and condensation Stefan problem

Fig. 7(A) shows the comparison between the numerical and analytical solutions. The red-solid and green-dashed lines denote the CFD results, whereas the black square denotes the analytical solution solved using Eq. (9). Overall, the numerical results obtained

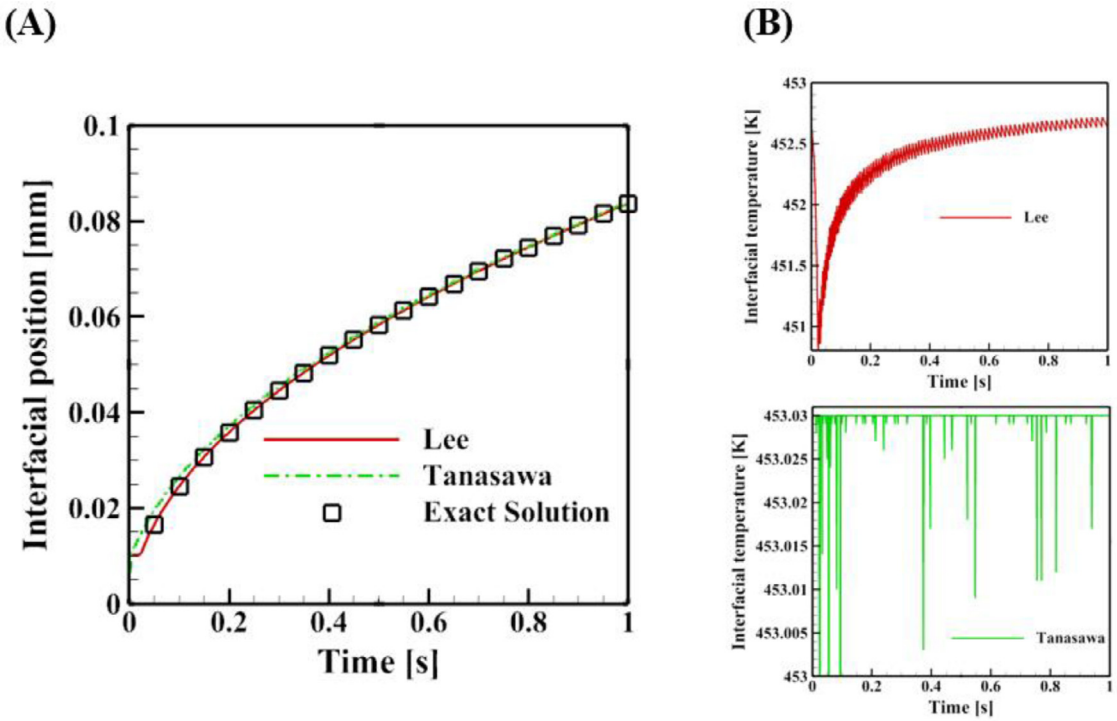

Fig. 8. Temporal result of the interfacial (A) position and (B) temperature for the condensation Stefan problem.

from the Lee and Tanasawa models were in a good agreement with the analytical solution. The interfacial position of the analytical solution at 1 s was 0.27 mm, whereas it was 0.271 and 0.272 using the Lee and Tanasawa models, respectively. Thus, the Lee model (0.37% error) performed slightly better than the Tanasawa model (0.74% error). Therefore, we conclude that both the solvers performed well in the evaporation problem. Fig. 7(B) shows the difference between the interfacial temperatures obtained from the two heat transfer models. A slight reduction in the interfacial temperature is observed in the Tanasawa model compared with the Lee model. This is because the Tanasawa model considers the saturation temperatures at both sides of the interface to be equal, so the interface temperature decreased to a value closer to the saturation temperature.

Fig. 8(A) shows the comparison of the interfacial position in the condensation Stefan problem. Similar to the evaporation case, the Lee and Tanasawa models well predicted the interfacial position compared with the exact solution. The Tanasawa model slightly overestimated the interfacial position compared with the Lee model. The error of the Tanasawa model relative to the analytical solution was 1.1%, whereas that of the Lee model was less than 0.1% at 1 s. Moreover, the interfacial temperature (see Fig. 8(B)) was significantly different between the two models. In the case of the Lee model, the interfacial temperature increased slightly as time progressed, which is reasonable considering that this is a condensation problem. By contrast, the Tanasawa model gave an interfacial temperature fluctuating around the saturation temperature.

Overall, in the evaporation problem, both models provided consistent results regarding the interfacial position compared with the exact solutions, whereas in the condensation case, the Lee model gave a slightly better result than the Tanasawa model. Consequently, we employed the Lee model in the following analysis to model the DCC-induced water hammer in the steam pipe because it is a condensation-dominant problem. Although we did not consider the Tanasawa model in our remaining simulations, performing more CFD simulations using both the Lee and Tanasawa models is recommended for a better understanding of the fundamental differences between the two models in a future study.

3.2. Grid convergence test

Fig. 9 shows the temperature behaviors and axial water velocity at a specific time (t = 8 s) inside the PMK-2 steam pipe at the measurement point T1 with two different grid types (A and B). The grid-type A is the medium non-uniform unstructured mesh shown in Fig. 5 with the standard wall function. The grid-type B is reconstructed by the structured mesh with a non-equilibrium wall function [32]. The numbers of cells in the grid-types A, and B are 2954,824, and 2997,504, respectively. As observed in Fig. 9, the temperature behaviors show a good agreement between the two types of grids. The temperature drops and their behaviors after dropping are almost consistent between the two grid types. This result suggests that both of the two grid types work well in capturing the water hammering effect. Besides, as observed in Fig. 9(D), the near-wall velocity as well as the velocity behaviors are also in a good agreement between the two grid types (A and B), ensuring a good validation at the near-wall behavior. The simulation times for the two types of grids were 49, and 65 h, respectively. However, the grid-type B shows more dynamic behaviors of the temperature than that of the grid-type A (see Fig. 9(A)). This could be due to the non-equilibrium wall function applied in the wall boundary condition. Therefore, a future study should be conducted to investigate the water hammering's sensitivity to the influence of turbulence, i.e., wall function. Somehow, in this study, we employed the grid-type A to simulate the water hammering phenomenon, which was generated by our semi-automatic mesh generation algorithm.

Fig. 10(A) shows the grid convergence tests for the PMK-2 case with three different grid sizes (coarse, medium, and dense grids) to ensure that all the solutions are satisfied with the given mesh size. We found that the results between medium and dense grids provide almost the same results at the temperature drop of the first measuring point (located 335 mm from the vertical pipe). In

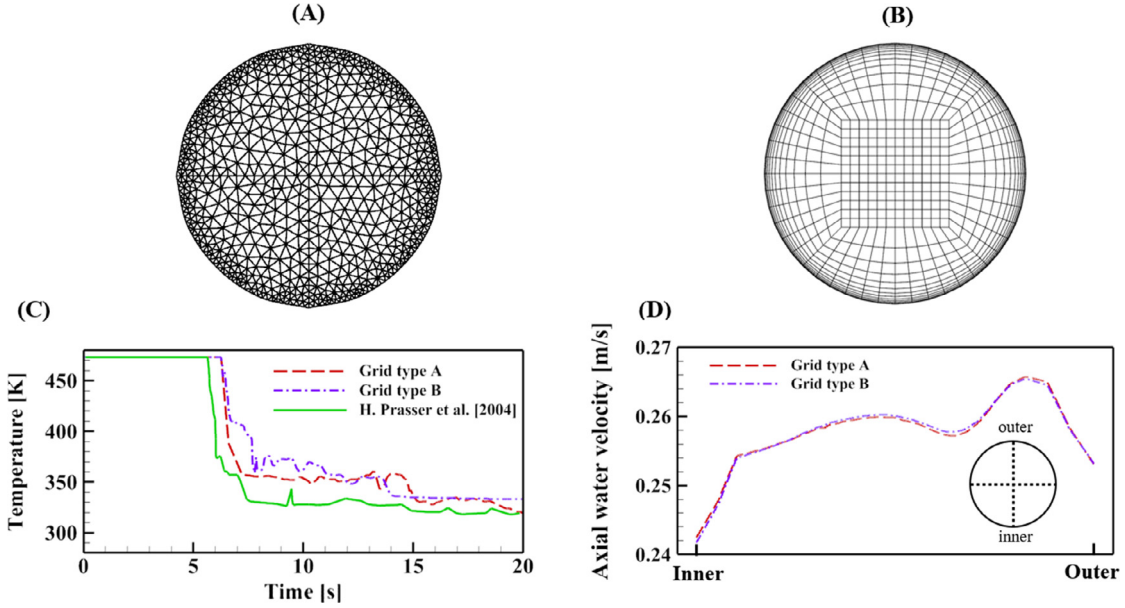

Fig. 9. (A) Unstructured mesh, (B) structured mesh, (C) temperature behaviors and (D) axial water velocity at the measurement point T1 at $t = 8$ s.

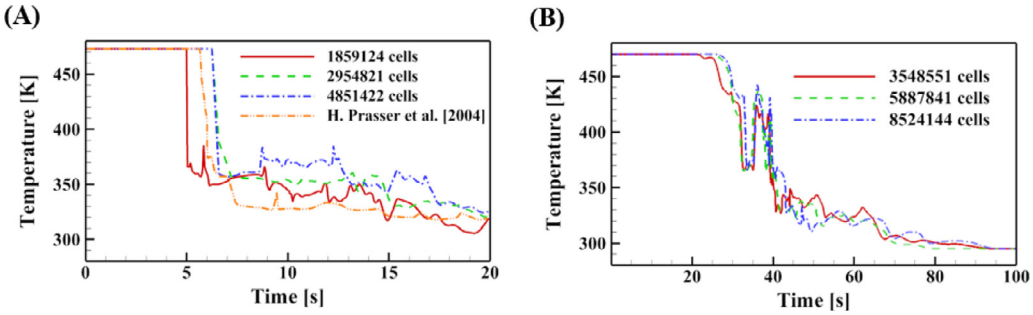

Fig. 10. Grid convergence test for the (A) PMK-2 and (B) KEPCO cases.

particular, compared with the experimental result, the three different grids had R^2 values of 0.85, 0.94, and 0.95, respectively. The simulation times for the three different grids were 45, 49, and 55 h, respectively. Based on the grid convergence test, the medium grid size was employed in this water hammering simulation of the PMK-2 case. The same process was followed for the KEPCO benchmark case. Similar to the PMK-2 case, the numerical simulations using both medium and dense grids provided almost the same results (see Fig. 10(B)); thus, a medium grid was chosen for the KEPCO case to ensure both numerical accuracy and computational cost.

3.3. Simulation of the DCC-induced water hammer in the PMK-2 experimental device

Fig. 11 shows the volume fraction of water and pressure contour inside the PMK-2 experiments captured at three different times ($t = 8.5$, 8.6, and 8.7 s). Initially, the water enters the test section as the subcooled water, and then the water and vapor coexist in a stratified flow regime. The condensation of vapor to water occurs continuously at the interface. Because of the phase change process, the steam loses its heat to the pipe wall and cooler condensate, in which the phase transitions from vapor to water and creates several steam pockets (Fig. 11(A)). Next, the condensation and flow of steam produce waves that build condensates until they fill the pipe cross section, trapping steam between water waves (Fig. 11(B)). Thereafter, this trapped steam condenses rapidly into water. This phenomenon then creates a much lower pressure zone than others and make the water move backward at a very high speed to fill out this void zone (Fig. 11(C)).

Fig. 12 shows the temperature behaviors inside the steam pipe at four measuring points with the current CFD, experimental, and previous CFD results. Overall, the CFD results in our study were in good agreement with the experiment results, especially for the time point where the temperature drops. At the T1 location (Fig. 12(A)), the temperature dropped at nearly 6.5 s from ~473 to ~330 K. The sudden drop in the temperature occurred 0.5 and 1.5 s later than the experiment in our CFD and existing CFD results [9], respectively. At the T2 location, the temperature drop was observed at 10.3 and 10.2 s in our results and the previous CFD results, respectively, which was observed at 9.6 s in the experiment. At the T3 location, the time point of the temperature drop was at 9.3 s in the experiment. The temperature drop was observed slightly later at 9.8 s in our CFD result, whereas it was observed at 11.7 s in the previous CFD result. At both T1 and T2, some temperature fluctuations were observed after the sudden drop in the temperature, which may indicate the water waves due to the flow instability. Finally, at the T4 location, the temperature drop was quite arbitrarily observed in the experimental results, our results, and previous CFD results. This implies that our CFD and previous CFD simulations could not accurately capture the temperature behaviors, such as temperature drop time and temperature peaks after several water hammering events. In summary, both CFD models fairly predicted the first sudden drop in temperature, but the tem-

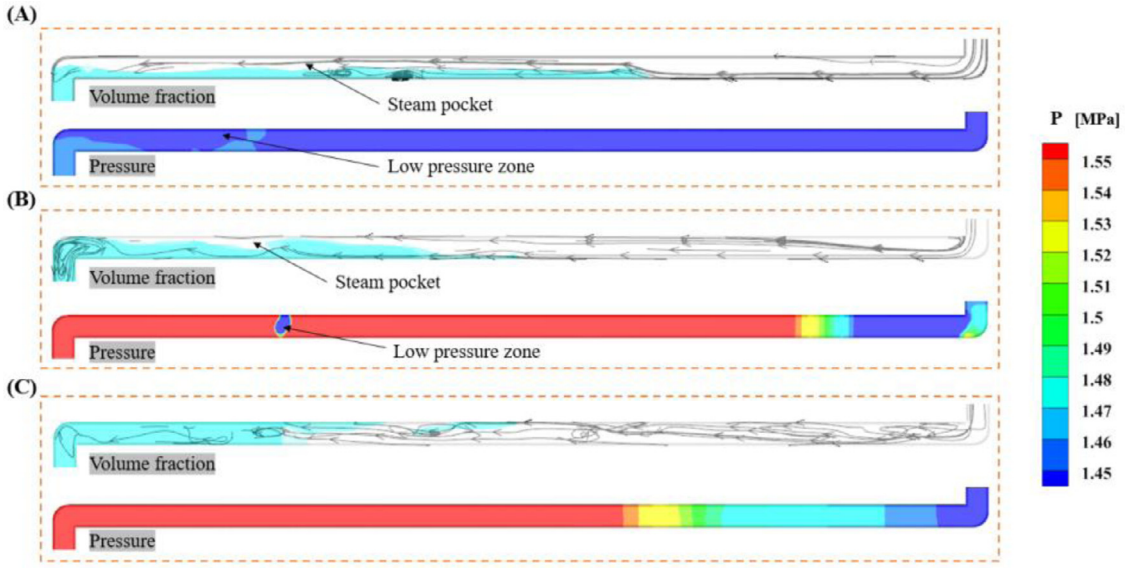

Fig. 11. Volume fraction of water and pressure contour inside the steam pipe at (A) 8.5, (B) 8.6, and (C) 8.7 s.

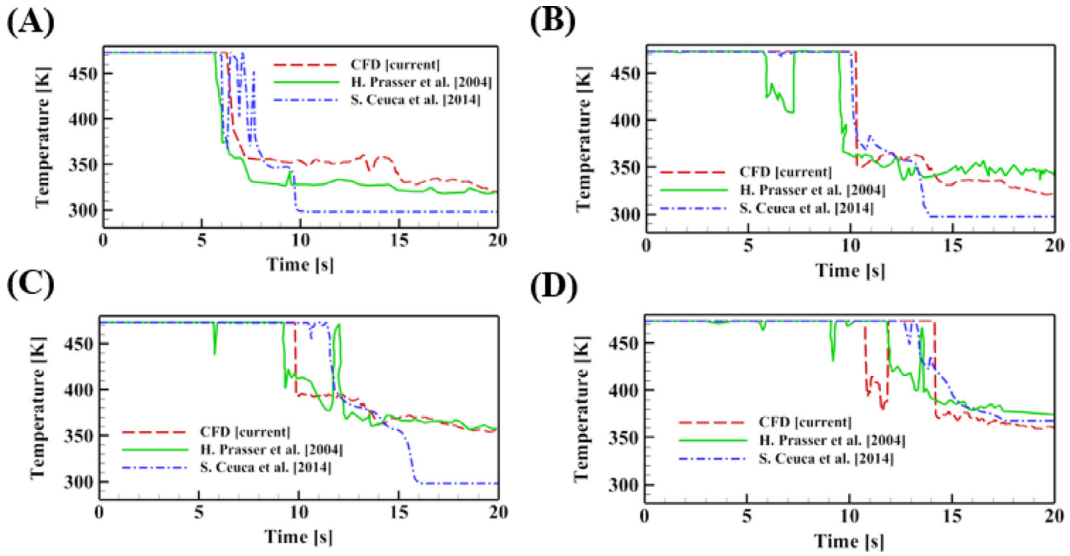

Fig. 12. Temperature behaviors inside the steam pipe at four measurement points: (A) T1, (B) T2, (C) T3, and (D) T4.

perature behaviors after the sudden drop were somewhat different from those in the experiment. This is possibly due to the sensitivity of the temperature value itself in the experimental measurements. Thus, a future study is needed to perform CFD simulation and experiments within well-designed conditions, such as boundary condition and numerical setting, to investigate the temperature behavior after the temperature drop.

We further measured pressures at two measurement points (Fig. 13). Note that the experimental article [8] did not report the pressures at these points. At the first measurement point, the maximum pressure peak of 11.2 MPa was observed, being nine times greater than the initial pressure of 1.45 MPa. As discussed above, the CIWH included a flow pattern change from horizontal to slug flow with a large steam bubble entrapment. The sudden condensation of this large steam pocket reduced the local pressure because the phase change of steam to water led to a volume reduction due to their density difference. The local void region due to the volume reduction then induced an adverse pressure gradient, so that the water front moved backward. The momentum energy of water

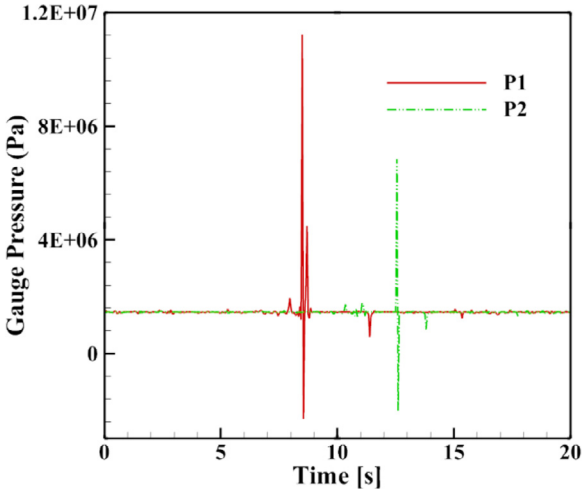

Fig. 13. Pressure behaviors inside the steam pipe at two measurement points.

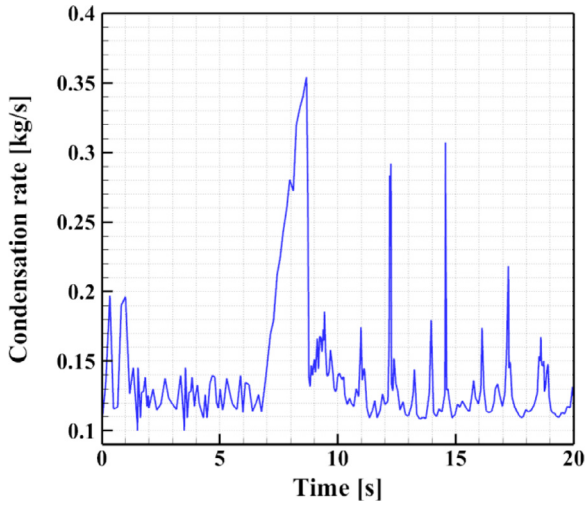

Fig. 14. Evolution of the volume-integrated condensation rate of the PMK-2 case.

turned into a sudden pressure surge. Relative to the first measurement point, a similar but weaker pressure peak was observed in the second measurement point, being five times greater than the initial pressure. This water hammering phenomenon continued until it reached the outlet.

The evolution of the volume-integrated condensation rate was described by employing the advantage of CFD (Fig. 14). From 0 to 1.5 s, the condensation rate increased when water moved in the horizontal section of the pipe. After 1.5 s, the condensation rate decreased because the water moved in the vertical pipe section. Following this, the condensation rate became maximum at 6 s in the horizontal section, which is consistent with the entrapping timing of vapor by the slug. We could also observe the low interfacial temperature at this time (Fig. 12(A)).

3.4. Simulation of the DCC-induced water hammer in a realistic KEPCO experimental steam pipe

We additionally performed CFD simulations, in which the geometry was obtained from an actual steam pipe of KEPCO. Fig. 15 shows the volume fraction of water, and pressure contour inside the steam pipe as time progresses. At $t = 37$ s, the subcooled water starts to enter the horizontal steam pipe. Similar to the PMK-2, the steam loses its heat to the pipe wall, so that a stratified flow regime is established between two phases and creates a wavy interface. After that, the relative velocity between two phases over the interface becomes substantial as the interfacial condensation rate is sufficiently high. Thus, because of the influences of the inertia force, the interface wave grows further enough such that the wave can touch the pipe wall at 38 s (Fig. 15(B)). Because of this phenomenon, the steam gets entrapped between the surrounding subcooled water slugs. This creates two zones: the low-pressure zone and high-pressure zone. Note that the low-pressure zone is also caused by the huge difference between the vapor and water volumes because their density ratio is quite large. This pressure jump causes a slug acceleration in the direction of the low-pressure zone, compressing the remaining steam, which finally collapses very rapidly and provides a pressure shock on the wall at $t = 39$ s.

The temperature and pressure values inside the steam pipe at two measurement points are shown in Fig. 16. At T1, the sudden decrease in temperature is observed, when the water comes in contact with the measurement point 1 at $t = 20.2$ s and $t = 37.8$ s at T2. The peak of the temperature is possibly due to an increase in condensation, corresponding to entrapped steam and water slug formation. Furthermore, the pressure evolution of the measure-

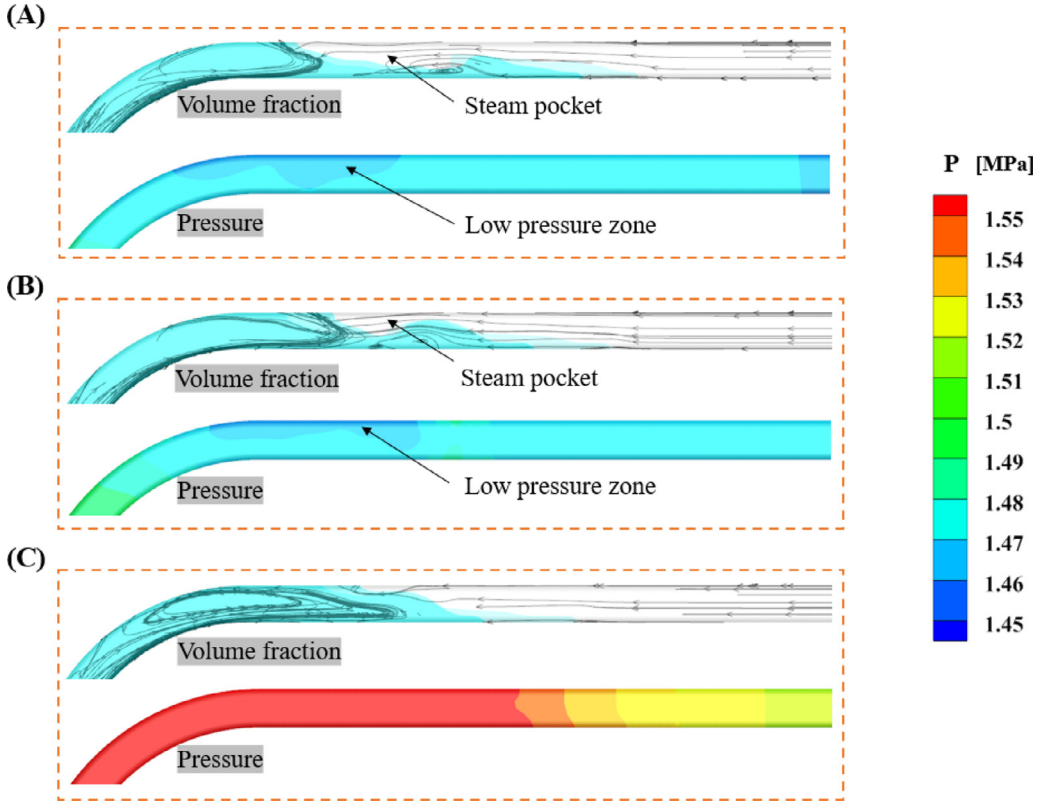

Fig. 15. Volume fraction of water and pressure contour inside the KEPCO steam pipe at (A) 37, (B) 38, and (C) 39 s.

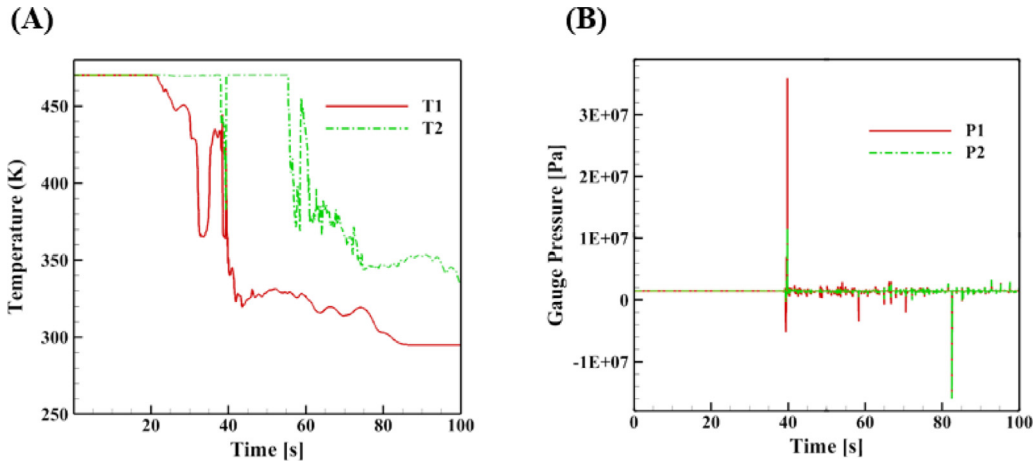

Fig. 16. (A) Temperature and (B) pressure behaviors inside the steam pipe at two measurement points.

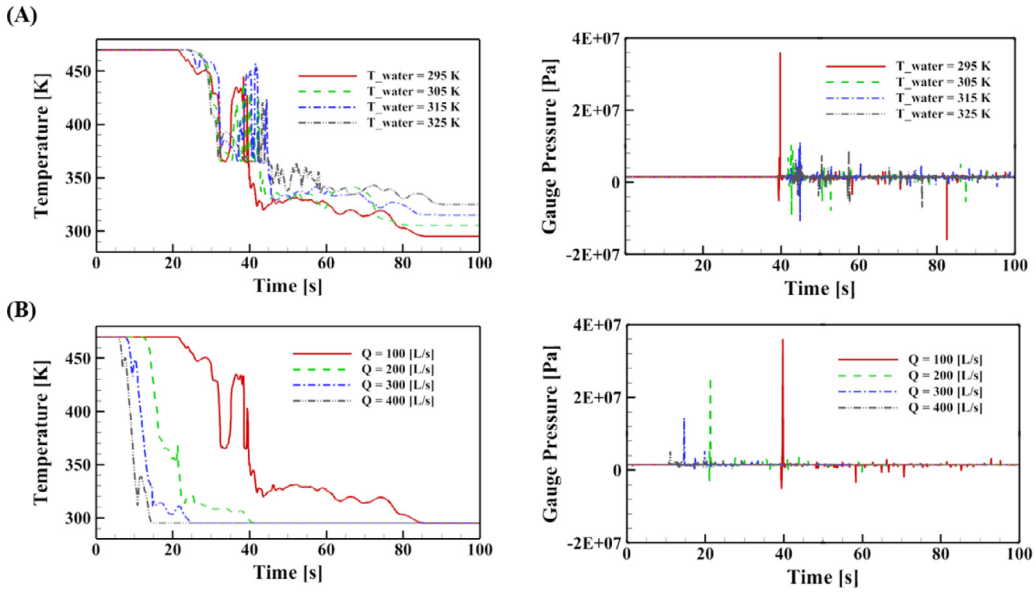

Fig. 17. Temperature and pressure behaviors inside KEPCO's realistic steam pipe at the first measurement point with different (A) water temperatures and (B) flow rates.

ment points is shown in Fig. 16(B). A pressure peak of around 35 MPa was recorded at 40 s, corresponding to a 24 time increase over the initial value of 1.45 MPa, possibly causing considerable damage to the pipe wall. This dangerous situation was caused by the sudden condensation of the large steam pocket. Different from the first measurement point, in the second measurement point, the pressure decreased 12 times relative to the initial value. Because the water filled up the pipe after the first water hammer happened, this situation continued until it reached the outlet. Consequently, the condensation was not as intense as the first water hammer and the pressure shock decreased. Overall, the flow physics of water hammering was consistent with the case of PMK-2, as described earlier.

3.5. Simulation of the DCC in the KEPCO steam pipe considering the change in flow rate and water inlet temperature

Fig. 17(A) shows the temperature and pressure behaviors inside the realistic KEPCO steam pipe at the first measurement point with different inlet water temperatures between 295 and 325 K. Because the water inlet temperature is not affected by the velocity, the water starts to meet the first measurement point within the steam pipe almost at the same instant as that for the different inlet water temperature around $t = 25$ s. However, a major deviation in the pressure profile is observed owing to the variation in water temperature. For $T_w = 295$ K, the pressure peak is nearly 24 times higher than the saturation pressure. However, it shows minor fluctuations in other water inlet temperatures; thus, the condensation is not as sudden as the first case of $T_w = 295$ K. An increase in the water temperature reduces the moving-back velocity as well as the water hammering effect in the steam pipe.

The effect of water injection velocity on the temperature and pressure behaviors is illustrated in Fig. 17(B). In the simulations, four different flow rates (100, 200, 300, and 400 L/s) were considered, resulting in Fr of 0.29, 0.59, 0.89, and 1.19, respectively. The water inlet temperature was maintained at 295 K. As the inlet flow rate increased from 100 to 400 L/s, the temperature dropped sooner because of the higher flow rate. Similar to the temperature behavior, the pressure behavior inside the steam pipe also shows a significant difference between the four flow rate (Q) values. In particular, as the Q increases, i.e., with fast water injection, the applied

pressure shock decreases to nearly zero for the case of $Q = 400$ L/s. In the fast injection, the water phase boundary was pushed as a column head, and thus stratification to slug flow regime transition did not occur, as observed in the case of $Q = 100$ L/s. Furthermore, we observed a significant temperature drop from 475 to 295 K, but the pressure did not change significantly. Therefore, an increase in the Q could be considered an important variable for mitigating the water hammer effect inside the steam pipe. This finding is aligned with the work of P. Griffith [33] because he also concluded that water hammer in the horizontal steam pipe could be avoidable under the condition of high water velocity (i.e., Fr $>$ 1).

4. Conclusions

The existing interFoam solver in the open-source software OpenFOAM was modified to simulate two-phase flow, including the phase change due to the temperature difference phenomenon. Semiautomated mesh-generation techniques were also utilized to take advantage of the easy production of the computational control surface and volume zones. The two-phase change models, i.e., the Lee and Tanasawa models, were coupled with the modified solver, which was further validated using the well-known 1-D condensation and evaporation Stefan problems. The Lee model showed better performance than the Tanasawa model, especially in the condensation case. Accordingly, the Lee model was utilized to describe the water hammer phenomenon in the steam pipes. First, the existing experiment using steam pipe PMK-2 provided by the Hungarian Atomic Energy Research Institute KFKI was employed to perform the phase change simulation. We found that the temperature drop from our CFD model was consistent with the experiment result and slightly better than the previous CFD result. However, the temperature behavior after the sudden temperature drop is somewhat different from the experiment, possibly because the sensitivity of the temperature value. Finally, the simulation of the water hammer was performed using a KEPCO steam pipe. It was found that the water started entering the horizontal steam pipe at 37 s, condensation occurred at 38 s, and ultimately collapsed at 39 s. The pressure shock was also observed to be 24 times higher than the initial value of pressure. In addition, different initial flow rates and water inlet temperature conditions were investigated to determine their effect on the water hammer phenomenon. We further demonstrated that the higher the value of the applied flow rate, the lower the pressure shock. Thus, the flow rate under these conditions may help alleviate the water hammer phenomenon. In our future endeavors, more complex parameters will be included in the simulation, including surface tension and fluid–structure interaction, to give more insights into the water hammer effect. Moreover, the performance of the parameter and shape optimization using deep learning techniques [34,35] could be considered to mitigate the water hammer.

Funding statement

This study was supported by the Korea Electric Power Corporation (KEPCO) [grant number R18XA06-67].

Declaration of Competing Interest

The authors declare that they have no known competing financial interests or personal relationships that could have appeared to influence the work reported in this paper.

CRediT authorship contribution statement

T.Q.D. Pham: Methodology, Software, Validation, Formal analysis, Investigation, Data curation, Writing – original draft. **Sanghun Choi:** Conceptualization, Resources, Writing – review & editing, Supervision, Funding acquisition.

References

[1] W.M. Rohsenow, J.P. Hartnett, E.N. Ganic, Handbook of Heat Transfer Applications, 1985.
[2] M.M. Rahman, J. Dongxu, M.S. Beni, H.C. Hei, W. He, J. Zhao, Supercritical water heat transfer for nuclear reactor applications: a review, Ann. Nucl. Energy 97 (2016) 53–65.
[3] H. Swidersky, Condensation induced water hammer (CIWH)–relevance in the nuclear industry and state of science and technology, J. Kerntechnik 78 (1) (2013) 16–21.
[4] G. He, M. Lin, B. Wang, Y. Liang, Q. Huang, Experimental and numerical research on the axial and radial concentration distribution feature of miscible fluid interfacial mixing process in products pipeline for industrial applications, Int. J. Heat Mass Transf. 127 (2018) 728–745.
[5] T. Poós, E. Varju, Mass transfer coefficient for water evaporation by theoretical and empirical correlations, Int. J. Heat Mass Transf. 153 (2020) 119500.
[6] R.W. Shumway, General features of emergency core cooling systems, in: Nuclear Power Safety, Elsevier, 1976, pp. 281–302.
[7] L. Štrubelj, G. Ézsöl, I. Tiselj, Direct contact condensation induced transition from stratified to slug flow, Nucl. Eng. Des 240 (2) (2010) 266–274.
[8] H. Prasser, G. Ezsol, G. Baranyai, PMK-2 water hammer tests, condensation caused by cold water injection into main steam-line of VVER-440-type PWR-Data Evaluation Report (DER), WAHALoads project deliverable D51, (2004).
[9] S.-C. Ceuca, Computational Simulations of Direct Contact Condensation as the Driving Force for Water Hammer, Technische Universität München, 2015.
[10] S.C. Ceuca, D. Laurinavicius, Experimental and numerical investigations on the direct contact condensation phenomenon in horizontal flow channels and its implications in nuclear safety, J. Kerntechnik 81 (5) (2016) 504–511.
[11] P. Datta, A. Chakravarty, K. Ghosh, A. Mukhopadhyay, S. Sen, A. Dutta, P. Goyal, Thangamani, modeling and analysis of condensation induced water hammer, Num. Heat Transf. 74 (2) (2018) 975–1000.
[12] T. Höhne, S. Gasiunas, M. Šeporaitis, Numerical modelling of a direct contact condensation experiment using the AIAD framework, Int. J. Heat Mass Transfer 111 (2017) 211–222.
[13] Y. Egorov, M. Boucker, A. Martin, S. Pigny, M. Scheuerer, S. Willemsen, Validation of CFD codes with PTS-relevant test cases, in: 5th Euratom Framework Programme ECORA project, 2004, pp. 91–116.
[14] E. Hughes, R. Duffey, Direct contact condensation and momentum transfer in turbulent separated flows, Int. J. Multiph. Flow 17 (5) (1991) 599–619.
[15] P. Coste, J. Pouvreau, J. Lavie´ville, M. Boucker, A two-phase CFD approach to the PTS problem evaluated on COSI experiment, in: International Conference on Nuclear Engineering, 2008, pp. 573–581.
[16] A.S. Rattner, S. Garimella, Simple mechanistically consistent formulation for volume-of-fluid based computations of condensing flows, J Heat Transf. 136 (7) (2014).
[17] H. Ganapathy, A. Shooshtari, K. Choo, S. Dessiatoun, M. Alshehhi, M. Ohadi, Volume of fluid-based numerical modeling of condensation heat transfer and fluid flow characteristics in microchannels, Int. J. Heat Mass Transf. 65 (2013) 62–72.
[18] Y. Sato, B. Ničeno, A sharp-interface phase change model for a mass-conservative interface tracking method, J. Comput. Phys. 249 (2013) 127–161.
[19] D. Sun, J. Xu, Q.J.N.H.T. Chen, Part B: fundamentals, Modeling of the evaporation and condensation phase-change problems with FLUENT, Num. Heat Transf. 66 (4) (2014) 326–342.
[20] J.H. Son, I.S. Park, Numerical simulation of phase–change heat transfer problems using heat fluxes on phase interface reconstructed by contour-based reconstruction algorithm, Int. J. Heat Mass Transf. 156 (2020) 119894.
[21] H. Lee, C.R. Kharangate, N. Mascarenhas, I. Park, I. Mudawar, Experimental and computational investigation of vertical downflow condensation, Int. J. Heat Mass Transf. 85 (2015) 865–879.
[22] W.H. Lee, Pressure iteration scheme for two-phase flow modeling, in: Multi-phase Transport: Fundamentals, Reactor Safety, Applications, 1980, pp. 407–432.
[23] I. Tanasawa, Advances in condensation heat transfer, in: Adv. Heat Transf, Elsevier, 1991, pp. 55–139.
[24] R.W. Schrage, A Theoretical Study of Interphase Mass Transfer, Columbia University Press, 1953.
[25] S. Chen, Z. Yang, Y. Duan, Y. Chen, D. Wu, Simulation of condensation flow in a rectangular microchannel, Chem. Eng. Process 76 (2014) 60–69.
[26] S.S. Deshpande, L. Anumolu, M.F. Trujillo, Evaluating the performance of the two-phase flow solver interFoam, Comput. Sci. Discov. 5 (1) (2012) 014016.
[27] H.G. Weller, A New Approach to VOF-based Interface Capturing Methods For Incompressible and Compressible Flow, 4, J OpenCFD Ltd., 2008 Report TR/HGW.
[28] B. Mohammadi, O. Pironneau, Analysis of the k-epsilon turbulence model, John Wiley and Sons, New York, NY, 1994.
[29] S. Miyawaki, E.A. Hoffman, C.-L. Lin, Numerical simulations of aerosol delivery to the human lung with an idealized laryngeal model, image-based airway model, and automatic meshing algorithm, Comput. Fluid. 148 (2017) 1–9.
[30] C. Geuzaine, J.F. Remacle, Gmsh: a 3-D finite element mesh generator with built-in pre-and post-processing facilities, Int. J. Numer. Method. Fluid. 79 (11) (2009) 1309–1331.

[31] L. Rubinšteĭn, The Stefan Problem, American Mathematical Soc., 2000.
[32] H.R. Nazif, H.B. Tabrizi, Applying a non-equilibrium wall function in k–ε turbulent modelling of hydrodynamic circulating flow, Appl. Math. Model. 38 (2) (2014) 588–598.
[33] P. Griffith, Screening reactor steam/water piping systems for water hammer, Nucl. Regul. Comm. (1997) Washington, DC (United States).
[34] R. Laubscher, P. Rousseau, Application of generative deep learning to predict temperature, flow and species distributions using simulation data of a methane combustor, Int. J. Heat Mass Transfer 163 (2020) 120417.
[35] C. Liu, W. Bu, D. Xu, Multi-objective shape optimization of a plate-fin heat exchanger using CFD and multi-objective genetic algorithm, Int. J. Heat Mass Transfer 111 (2017) 65–82.